Supplementary Material (ESI) for Journal of Materials Chemistry

Supplementary Information: Inhomogeneous Composition of Alloyed Iron-Platinum Magnetic Nanoparticles Synthesized at Low Temperature

Shu Chen, Donald A. MacLaren, Richard T. Baker, John N. Chapman, David J. Cole-Hamilton, Stephen Lee, Pascal André *

* Pascal.Andre@st-andrews.ac.uk

SI-I. Experimental Section

SI-I.1. Materials

All chemical reagents, unless otherwise stated, were purchased from Sigma (Poole, UK). All chemicals were degassed before use. Iron (III) chloride ($FeCl_3$, reagent grade, 97 %), iron (II) chloride ($FeCl_2$, anhydrous, beads, 99.9 % trace metals basis), iron (II) acetate ($Fe(CO_2CH_3)_2$, 99.995 % trace metals basis), Iron(III) nitrate nonahydrate ($Fe(NO_3)_3 \cdot 9H_2O$, ACS reagent, ≥ 98 %), potassium tetrachloroplatinate (II) (K_2PtCl_4, 98 %), sodium hexachloroplatinate (IV) hexahydrate ($Na_2PtCl_6 \cdot 6H_2O$, 98 %), hydrazine monohydrate ($N_2H_4 \cdot H_2O$, reagent grade, 98 %), sodium borohydride ($NaBH_4$, ReagentPlus®, 99 %), polyethylene glycol hexadecyl ether, Brij52 ($C_{16}H_{33}(OCH_2CH_2)_2OH$, average M_n ~330 kD), 1-dodecane thiol ($CH_3(CH_2)_{11}SH$, ≥ 98 %), isooctane (ACS reagent, ≥ 99.0 %), hexane (ACS reagent, 99.0 %), ethanol (ACS reagent, ≥ 99.5 %), methanol (ACS reagent, ≥99.8 %), HCl (Trace SELECT®, ≥ 37 %) HNO_3 (Trace SELECT®, ≥ 69.0 %)

SI-I.2. Synthesis

In a typical synthesis, a surfactant (Figure 1A) solution (0.3 mol/L) was prepared by mixing isooctane (20 mL), Brij52 (1.98 g, 0.3 mol/L) and butanol (110 µL) in a surfactant to alcohol ratio of 5:1. Dissolution was obtained after 15 min sonication. K_2PtCl_4 (277 mmol/L) and $FeCl_3$ (277 mmol/L) aqueous stock solutions were added to the amphiphilic system to obtain equal $[Pt^{2+}]$ and $[Fe^{3+}]$ concentration (2.5 mmol/L). 30 min sonication was then applied, followed by injection of $N_2H_4.H_2O$ to reach a molar ratio of $[N_2H_4.H_2O]$ / [Fe+Pt] = 40. The hydration, *w*, is the molar ratio of water to surfactant molecules,

$$w = [H_2O] / [\text{Brij52}] \quad (1)$$

and the final *w* value equal to 4 is reached after addition of hydrazine monohydrate. The system was stirred at 30 ºC for 3 h. Dodecane thiol was then injected and the solution aged for further 15 min. The nPs were then precipitated by adding alcohol, and collected by centrifugation. This extraction step was repeated several times. A similar protocol was followed when the syntheses were completed with different iron and platinum precursors, and a different reducing agent.

SI-I.3. Characterization Techniques

Impedance spectroscopy was used to quantify the electrical conductivity of the amphiphilic solutions. All samples had a surfactant concentration of [Brij52] = 0.3 mol/L, and a surfactant to co-surfactant ratio of [Brij52] / [butanol] = 5. Water content, *w*, was varied from 1 to 6. The investigation of electrochemical properties of non-ionic amphiphilic systems is notoriously difficult due to the lack of charge carriers. Therefore a dilute salt solution (10^{-3} mol/L NaCl in this work) is typically used instead of water to provide sufficient charge carriers to allow a detectable signal to be obtained while making sure the chemical phase behavior is not affected.[1] The electrochemical test cell consisted of two disk-shaped electrodes within a thermally regulated cylindrical container. The test sample was placed between these electrodes and the height of the upper electrode was adjusted to bring it into contact with the upper surface of the solution to be tested. The temperature was controlled at 30 ± 1 ºC using a closed loop circulating water heating system.

Impedance can be expressed as the sum of a real (Z') and an imaginary (Z'') component:

$$Z = Z' + jZ'' \quad (2)$$

Z' relates to the resistive properties of a sample while Z'' is related to the reactive elements, that is capacitances and inductances. Impedance spectra are obtained by sweeping the frequency over a wide range, so causing variations in the values of Z', Z'' and Z.[2] Such spectra are conveniently presented as so-called Nquist plots in which Z'' is plotted against Z'. Such impedance spectra were obtained using a Solartron 1260 Frequency Response Analyser operating in two-electrode mode and run using ZPlot software. An a.c. potential of amplitude 400 mV was applied over a frequency range of 0.5 Hz to 1 MHz. The resulting Nquist spectra contained approximately semicircular features which can be fitted to an equivalent electronic circuit model consisting of a resistance, *R*, and a capacitance, *C*, connected in parallel. The distance between the two intercepts of the semicircular arc with the Z' axis gives the value of *R*. *C* is related to the value of signal frequency, *f* (Hz), at the maximum height of the arc where: [2-3]

$$C = \frac{1}{2\pi f R} \quad (3)$$

Values of *R* and *C* were extracted from the impedance data using this fitting procedure in the ZView software package. The conductivity *k* (*S*/cm) of the solutions were calculated according to the following equation:[3]

$$k = \frac{d}{AR} \quad (4)$$

where *d* (cm) is the distance between the electrodes and *A* (cm^2) the effective area of the electrodes. In this experiment, the electrode radii were 1 cm and the distance between the electrodes was set to 0.3 cm. Standard deviation values of the conductivity were obtained by repeating each impedance measurement 3 times and fitting each resulting spectrum separately.

Inductively coupled plasma optical emission spectroscopy (ICP-OES) measurements were completed with a Perkin Elmer Optima 5300 DV spectrometer. FePt nPs were dissolved overnight at room temperature by addition of hydrochloric acid

and nitric acid mixed in 3:1 volume ratio (aqua regia). After full dissolution of the nPs, the solutions were further diluted with deionised water.

Wide-angle powder X-ray diffraction (XRD) spectra were collected on a Stoe STADI/P powder diffractometer operating in transmission mode and with a small angle position sensitive detector. The peaks were fitted by Lorentzians with STOEwinXpow and Kaleida-Graph software to determine the peak positions and width. The crystalline grain size equivalent to the "average" diameter of the crystallites, D_{XRD}, of the FePt nPs was calculated according to Scherrer's formula:

$$D_{XRD} = 0.9\lambda/(B \cos\theta) \quad (2)$$

where λ =1.936 Å corresponding to the wavelength of the incident X-ray radiation generated using a $Fe_{K\alpha 1}$ source, B is the full width at half maximum of the peak intensity (FWHM), θ is the glancing angle.[4] D_{XRD} is determined based on (111), (200) and (220) peaks.

The atomic composition of FePt nPs was calculated based on the linear relations between lattice constant, a, and Fe percentage, Fe %, reported on *fcc*-FePt lattice constant (SI-Figure 1).[5]

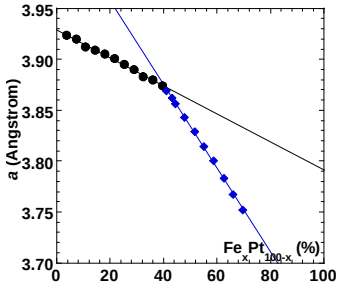

SI-Figure 1. FePt lattice constant (a) analysed by XRD vs. composition curve reported by Bonakdarkpour et al.[5]

SI-Figure 1 leads to the following equations:

$x_{\%Fe} < 40$ % $\quad a = -0.0014\, x_{\%Fe} + 3.929$ eq. (1)

$x_{\%Fe} > 40$ % $\quad a = -0.0041\, x_{\%Fe} + 4.039$ eq. (2)

It is noticeable that the alloys used by Bonakdarkpour et al were prepared by sputtering of Fe and Pt sources. Ideally nanoparticles and not films would have been used for us to compare with. However, at the moment, there is not a consistent set of data available in the literature covering both size, composition and surface chemistry of colloidal FePt nPs. At the current stage of development of FePt alloy nPs controlling the size and composition is already a challenge, as illustrated by our report, and using vacuum depositing films of Fe_xPt_{1-x} provides the most reliable reference to compare our material with.

In our study, a was determined based on (111), (200) and (220) peaks to reduce potential risks of systematic error compared to a single peak analysis, alternatively a Rietveld approach could have been used even though it would have been more time consuming without necessarily increasing the data precision.[6]

Transmission electron microscopy (TEM) was conducted on an FEI Tecnai F20 transmission electron microscope that is equipped with a field emission gun operated at 200 kV. Size distribution analysis was completed by computer assister image analysis and only on the areas of the TEM grid which presented well dispersed nPs. In contrast, the TEM grid areas of large aggregation were not used for this analysis. As always, when dealing with quantitative size distribution obtained by TEM one should be especially careful and the radius population is given for guide only.

Energy dispersive X-Ray (EDX) analysis was performed in both conventional TEM and **scanning TEM** (STEM) modes using an energy dispersive X-ray spectrometer. Fe and Pt composition ratios were determined by comparing the intensity of K_α and L_α EDX peaks, respectively, with those collected from a thin film FePt sample of known stoichiometry.[7]

Nanometer scale scanning transmission electron microscopy and energy dispersive X-ray (nanoSTEM-EDX) was used to obtain the bright/dark field of image (SI-Figure 2A and B, respectively) of a well-characterised FePt($L1_0$) - 1:1 Fe:Pt ratio - grown by molecular beam epitaxy (MBE) on MgO substrate. FePt sample appeared as darker contrast in bright field image, SI-Figure 2A, and brighter contrast in dark field image, SI-Figure 2B. The red box in SI-Figure 2B indicates the area from where the nanoSTEM-EDX spectrum was obtained. The reference spectrum was shown in SI-Figure 2C, the ratio of Fe K_α at 6.398 keV and Pt L_α at 9.441 keV is about 0.8 and was used as a reference to determine the composition of FePt nPs samples at a nanometer scale and a potential 'shadow effect' altering the nanoSTEM-EDX spectra can be excluded because of the small size of the nPs.

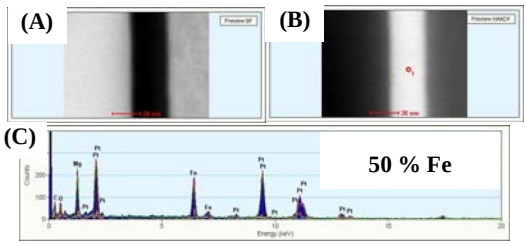

SI-Figure 2. Bright field STEM picture (A), corresponding dark field image with red squares indicating areas analyzed by nanoSTEM-EDX (B) and EDX spectra (C) of a 1:1 Fe:Pt ratio MBE-grown FePt($L1_0$)/MgO sample

The results are consistent with homogenous sample obtained by thermal decomposition protocol and characterized by XRD, EDX, and IPC-EOS.

False-coloured energy filtered TEM (EF-TEM) was conducted on an FEI Tecnai T20 transmission electron microscope equipped with a Gatan Imaging Filter. False-coloured maps were obtained by using the Pt-$M_{4,5}$ and Fe-$L_{2,3}$ electron energy loss (EELS) edges, respectively, to map Pt and Fe elemental distributions.

A **superconducting quantum interference device** (SQUID magnetometer MPMS XLTM from Quantum Design) was used to characterize the nPs magnetic properties. Zero-Field Cooled and Field Cooled (*ZFC*/*FC*) measurements were completed as follow: the sample was first cooled from room temperature to 5 K without applying any external field, next a small field 100 Oe was applied and the magnetization of nPs was recorded as the temperature was slowly increased to 275 K. The *FC* curve was obtained by cooling the sample back to 5 K while the same external field of 100 Oe was applied. The magnetization was then measured as the temperature was slowly increased to 275 K. Hysteresis measurements were completed at temperatures of 5 K and 300 K with an external field sweep from -5 to 5 Tesla.

SI-II. Precursors ratio and $N_2H_4.H_2O$ as reducing agent

SI-II.1. Electron diffraction composition data analysis

SI-Figure 3 presents TEM images of FePt nPs synthesized with different precursor ratio. All the nanoparticles have a similar 'cauliflower - knobbly' morphology and appear poly-

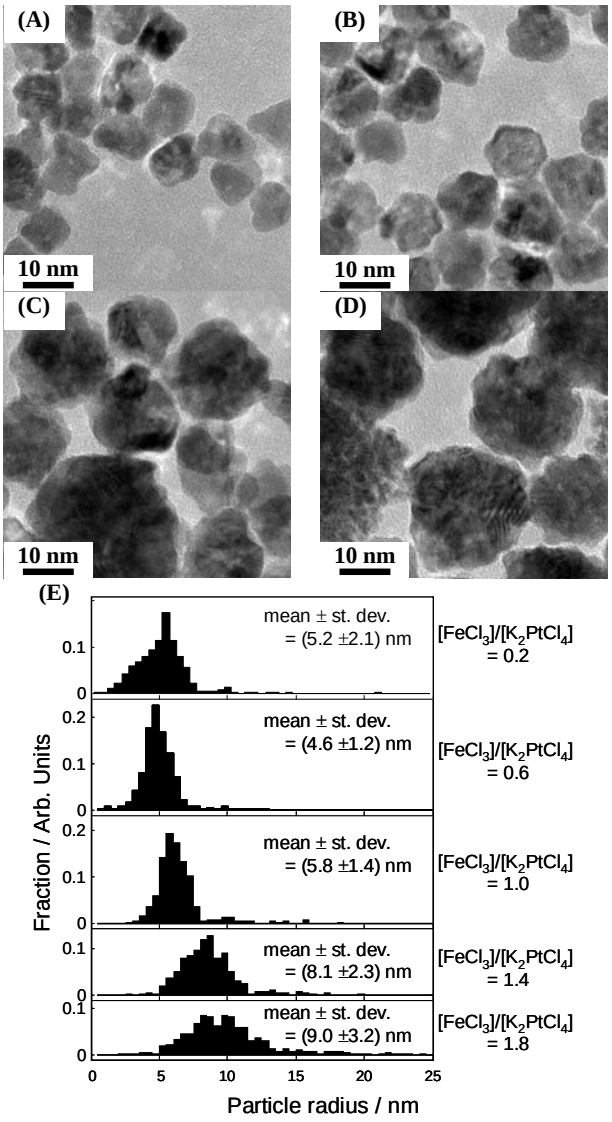

SI-Figure 3. TEM images of FePt NPs synthesized at 30°C in isooctane, [Brij52] = 0.3 mol/L, [Brij52] / [butanol] = 5, w = 4, [K_2PtCl_4] = 2.5 mmol/L and [$N_2H_4.H_2O$] / [Fe^{3+}+Pt^{2+}] = 40. [$FeCl_3$] to [K_2PtCl_4] molar ratio from 0.6 (A), 1.0 (B), 1.4 (C), 1.8 (D) and their TEM size distribution in radius.

domain. This aspect may well have arisen from the coalescence of smaller particles during synthesis (SI-Figure 3A-D). This is consistent with the smaller nPs crystalline size revealed by XRD (Table 1) than TEM size (SI-Figure 3E). The TEM size of nPs increases with the Fe to Pt precursor ratio, as shown in SI-Figure 3E. This could be attributed to a reduction of the pH with increasing Fe precursor concentration which would weaken the strength of hydrazine and lead to a slower nucleation rate, therefore larger nPs.

SI-Figure 4 shows electron microscopy analysis of FePt nPs synthesized in amphiphilic system by co-reduction with hydrazine monohydrate. The rows 1 to 5 correspond to FePt nPs synthesized with increasing the Fe to Pt precursor ratio as reported in Figure 4 of the main document. In SI-Figure 4, the left hand side column (A1-A5) presents the transmission electron microscopy images while the right hand side column (B1-B5) show the associated electron diffraction (TEM- ED) patterns. The nanoparticles appear polydisperse and with a size

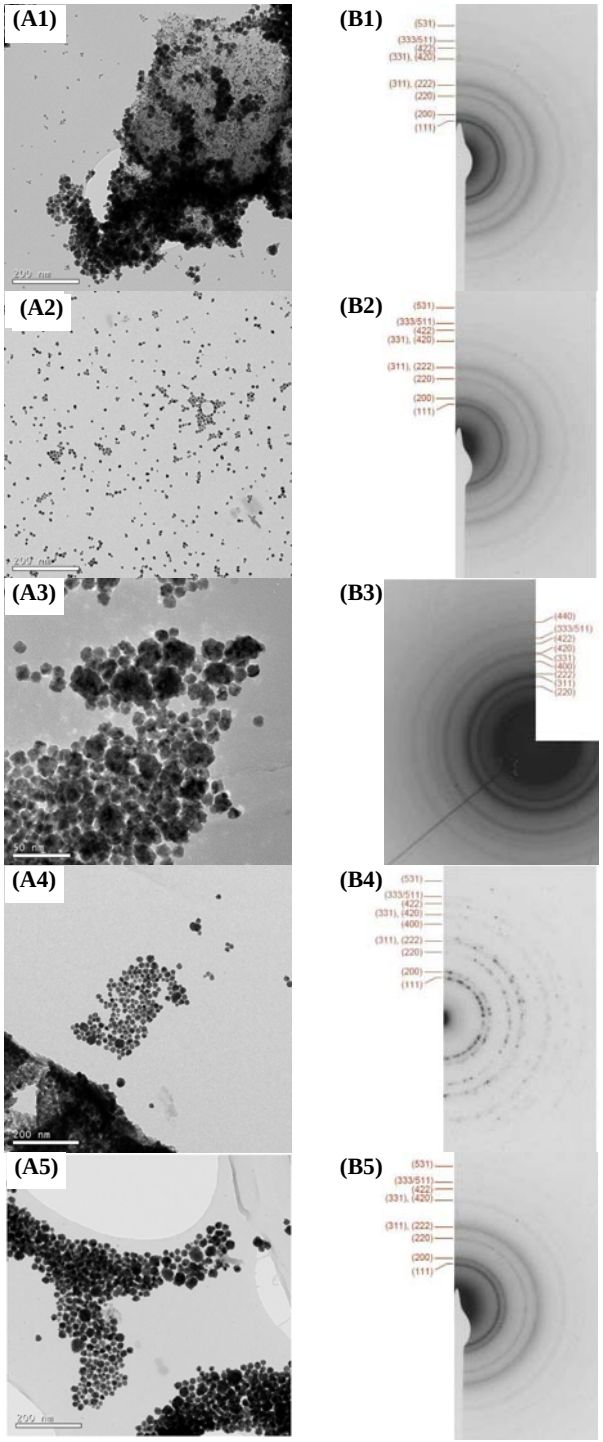

SI-Figure 4. TEM image (A) and corresponding selected area electron diffraction pattern (B) of FePt NPs synthesized at 30° C in isooctane, [Brij52] = 0.3 mol/L, [Brij52] / [butanol] = 5, w = 4, [K_2PtCl_4] = 2.5 mmol/L and [$N_2H_4.H_2O$] / [Fe^{3+}+Pt^{2+}] = 40. [$FeCl_3$] to [K_2PtCl_4] molar ratio from 0.2 (1), 0.6 (2), 1.0 (3), 1.4 (4) and 1.8 (5).

increasing with the Fe to Pt precursors ratios. Regardless of the initial Fe to Pt precursor ratio, the rings observed in the electron diffraction patterns can be assigned to *fcc*-FePt crystal structure consistent with the X-Ray Diffraction data presented in Figure 3 and Table 1 of the main document.The lattice constant of the FePt nPs calculated from the TEM-EDX data (SI-Figure 4B) are presented in SI-Figure 5.

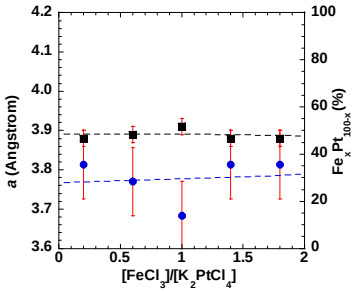

SI-Figure 5. TEM-ED results as a function of Fe to Pt ratio in the FePt nPs syntheses with varied $FeCl_3$ concentration at 30° C in isooctane, [Brij52] = 0.3 mol/L, [Brij52] / [butanol] = 5, w = 4 and $[N_2H_4.H_2O]$ / $[Fe^{3+}+Pt^{2+}]$ = 40. Lattice constant (■) and chemical composition (●) deduced from electron diffraction analysis.

Regardless of the initial Fe to Pt precursor ratio, all the FePt nPs samples have a lattice constant varying between 3.88 and 3.92 ± 0.02 Å. As deduced from SI-Figure 1 and eq (1-2), the corresponding chemical compositions would vary from 15 to 35 % with a large error bar of about 15 %. In the present experiments, the uncertainty associated with the determination of the lattice constant obtained from TEM-ED is much larger than with XRD presented in Figure 3 and Table 1.

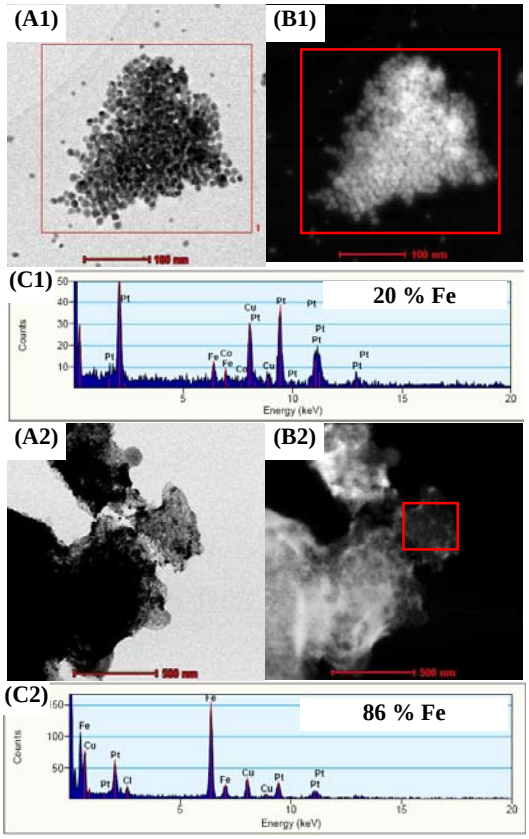

SI-Figure 6. Bright field TEM picture (A), corresponding dark field image with red squares indicating areas analyzed by nanoSTEM-EDX (B) and EDX spectra (C) of FePt nPs synthesized at 30° C in isooctane, [Brij52] = 0.3 mol/L, [Brij52] / [butanol] = 5, w = 4, $[N_2H_4.H_2O]$ / $[Fe^{3+}+Pt^{2+}]$ = 40. Molar ratio of Fe to Pt precursor = 0.2.

SI-II.2. nanoSTEM-EDX Composition

SI-Figure 6 shows nanoSTEM-EDX data of FePt nPs synthesized with initial 0.2:1 molar ratio of Fe to Pt precursor. SI-Figure 6A1 show well dispersed nPs with dark contrast. SI-Figure 6B1 shows the equivalent image in dark field. The nPs appear to be crystalline while the composition is Pt rich (SI-Figure 6C1). The Fe is found in the film-like material, with typical data shown in SI-Figure 6A2-B2. The nPs appear to be more crystallized than the film like materials as illustrated by the dark field STEM image (SI-Figure 6C). This is consistent with the XRD spectra.

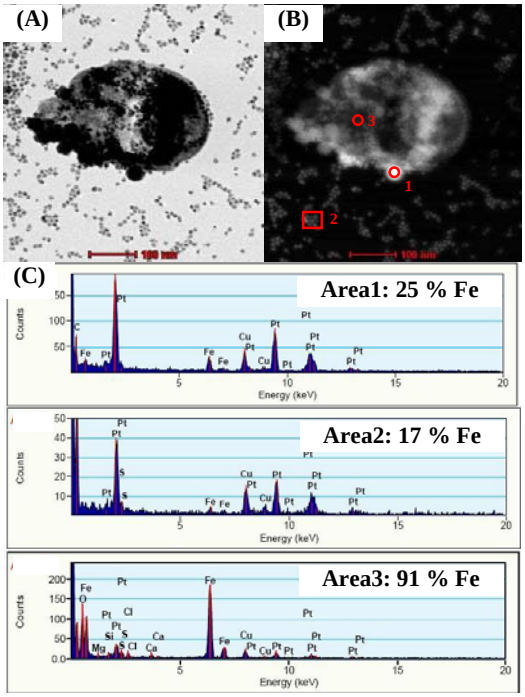

SI-Figure 7. Bright field STEM picture (A), corresponding dark field image with red squares indicating areas analyzed by nanoSTEM-EDX (B) and EDX spectra (B) of FePt nPs synthesized at 30° C in isooctane, [Brij52] = 0.3 mol/L, [Brij52] / [butanol] = 5, w = 4, $[N_2H_4.H_2O]$ / $[Fe^{3+}+Pt^{2+}]$ = 40. Molar ratio of Fe to Pt precursor = 0.6.

SI-Figure 7 displays nanoSTEM-EDX data of FePt nPs synthesized with initial 0.6:1 molar ratio of Fe to Pt precursor. Well dispersed nPs as well as film-like materials are also shown in SI-Figure 7A-B. The nPs are relatively polydisperse in size (SI-Figure 7A-B), Pt rich (SI-Figure 7C) and apparently inhomogeneous in composition (SI-Figure 7C). Film-like material is Fe rich, trace of oxygen and chlorine may suggest the incomplete reduction of Fe precursor, or the hydrolysis product of Fe salt β-FeOOH (SI-Figure 7C).

SI-Figure 8 presents nanoSTEM-EDX data of FePt nPs synthesized with initial 1:1 and 1.4:1 molar ratio of Fe to Pt precursor. nP contain 17 to 22 % of Fe (SI-Figure 8A1-C1 and A2-C2, Area 1). Again the samples appear inhomogeneous in composition. Fe was found in film material, as shown in SI-Figure 8A1-C1 and A2-C2, Area 2.

SI-Figure 9 shows show similar results even though the synthesis was carried out with a much larger initial Fe to Pt precursor ratio. Again Fe material can be found in the film-like material which also contains trace of Oxygen and Chlorine (SI-Figure 9C2), this is consistent with the other samples. As mentioned above, Oxygen and Chlorine could be associated with the incomplete reduction of the Fe precursor, or the hydrolysis of Fe salt into β-FeOOH. The latter can be described

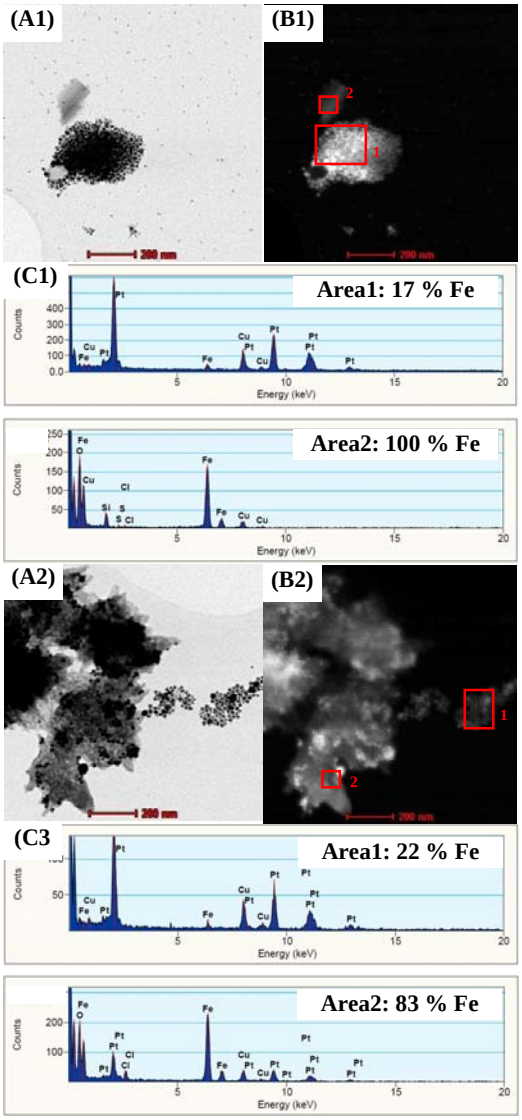

SI-Figure 8. Bright field STEM picture (A), corresponding dark field image with red squares indicating areas analyzed by nanoSTEM-EDX (B) and EDX spectra (C) of FePt nPs synthesized at 30° C in isooctane, [Brij52] = 0.3 mol/L, [Brij52] / [butanol] = 5, w = 4, [$N_2H_4.H_2O$] / [Fe^{3+}+Pt^{2+}] = 40. Molar ratio of Fe to Pt precursor = 1.0 (A1 to C1), and = 1.4 (A2 to C2).

by the following reaction Equations (1-6):[8]

$$Fe^{3+} + H_2O \rightarrow FeOH^{2+} + H^+ \quad (1)$$

$$FeOH^{2+} + H_2O \rightarrow Fe(OH)^{2+} + H^+ \quad (2)$$

$$Fe(OH)^{3+} + H_2O \rightarrow Fe(OH)_3 + H^+ \quad (3)$$

$$Fe(OH)_3 + H_2O \rightarrow Fe(OH)_4^- + H^+ \quad (4)$$

$$2Fe^{3+} + 2H_2O \rightarrow Fe_2(OH)_2^{4+} + 2H^+ \quad (5)$$

$$3Fe^{3+} + 3H_2O \rightarrow Fe^3(OH)_4^{5+} + 4H^+ \quad (6)$$

These hydrolysis reactions of $FeCl_3$would then be associated with a pH reduction, which was indeed observed experimentally. To mimic synthesis condition, all solutions were aged for about 20 min at 30 ºC before completing the pH analysis, while [Fe^{3+}] and [Pt^{2+}] were adjusted to be as the same as [Fe^{3+}] and [Pt^{2+}] in the water phase of the amphiphilic system used to carry out the nPs synthesis. The results are presented in SI-Table 1. While K_2PtCl_4 aqueous solution at 0.14 M [Pt^{2+}] has a pH of 4.0 when no $FeCl_3$ is present, pH tends to decrease as [$FeCl_3$] is increased until it saturates at pH = 1.2.

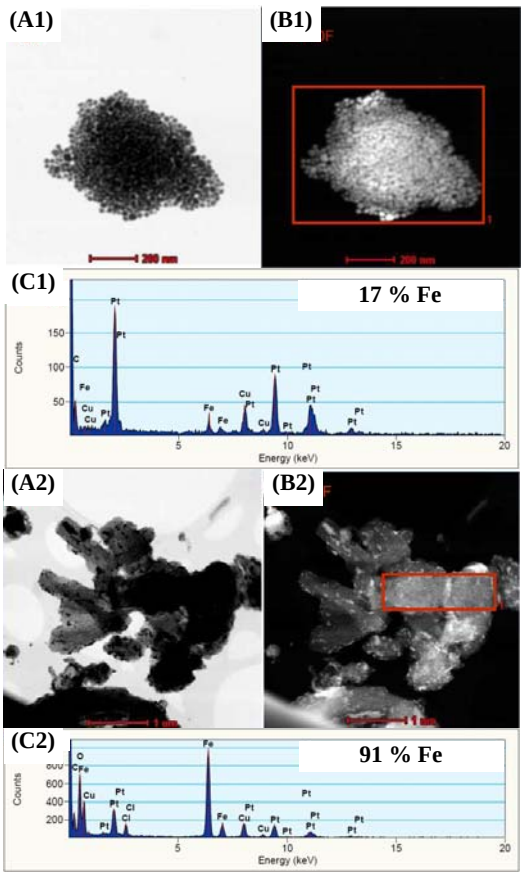

SI-Figure 9. Bright field STEM picture (1), corresponding dark field image with red squares indicating areas analyzed by nanoSTEM-EDX (2) and EDX spectra (3) of FePt nPs synthesized at 30° C in isooctane, [Brij52] = 0.3 mol/L, [Brij52] / [butanol] = 5, w = 4, [$N_2H_4.H_2O$] / [Fe^{3+}+Pt^{2+}] = 40. Molar ratio of Fe to Pt precursor =1.8.

SI-Table 1. pH analysis on solutions containing varied molar ratio of $FeCl_3$ and K_2PtCl_4.

Solution	pH
K_2PtCl_4	4.0
[$FeCl_3$]/[K_2PtCl_4]=0.2	2.2
[$FeCl_3$]/[K_2PtCl_4]=0.6	1.6
[$FeCl_3$]/[K_2PtCl_4]=1.0	1.4
[$FeCl_3$]/[K_2PtCl_4]=1.4	1.3
[$FeCl_3$]/[K_2PtCl_4]=1.8	1.2
$FeCl_3$	1.2

SI-III. Reaction Time / Pt-Fe Precursors / Reducing Agent

SI-III.1. General Comments

From SI-Table 2, it is noticeable that the difference of redox potentials between the Pt salt and hydrazine monohydrate (0.985 V) is much larger than the difference of potential between Fe^{3+} and hydrazine monohydrate (0.193 V), supporting a stronger and faster reduction of Pt^{2+} than Fe^{3+}. In addition, rather than being directly reduced from Fe^{3+} to Fe^0, (-0.037 V), a partial reduction to Fe^{2+} will occur which will next be reduced to Fe^0 with still a weaker strength than $[PtCl_4]^{2-}$ being reduced to Pt^0.

Complication could arise with on the one hand Pt metal acting as catalyst and contributing to the reduction of Fe ions as observed in other systems,[10] and on the other hand the formation of yellow precipitates which can be observed within

SI-Table 2. Decreasing Standard redox potentials.[9]

Chemical Reaction	E° (V)
$[PtCl_4]^{2-} + 2e^- \leftrightarrow Pt^0 + 4Cl^-$	0.755
$[PtCl_6]^{2-} + 2e^- \leftrightarrow Pt^0 + 6Cl^-$	0.68
$Fe^{3+} + 3e^- \leftrightarrow Fe^0$	-0.037
$N_2H_4.H_2O \leftrightarrow N_2 + 5H^+ + 4e^- + OH^-$	-0.23
$Fe^{2+} + 2e^- \leftrightarrow Fe^0$	-0.447
$Fe^{3+} + e^- \leftrightarrow Fe^{2+}$	-0.771
$BH4^- + 3H_2O \leftrightarrow B(OH)_3 + 7H^+ + 8e^-$	-1.73

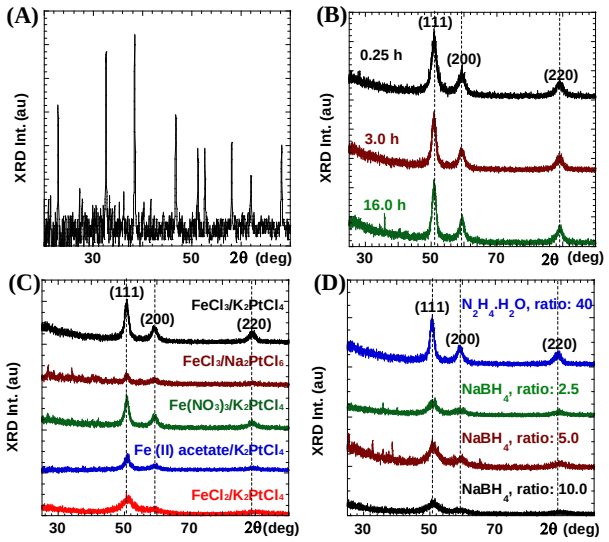

SI-Figure 10. XRD patterns of yellow precipitates formed by mixing of $FeCl_3$ and K_2PtCl_4 aqueous solution directly at 30 ºC, $[Fe^{3+}] = [Pt^{2+}] = 0.14$ M (A); FePt NPs synthesized at 30°C in isooctane, [Brij52]=0.3 mol/L, [Brij 52]/[butanol]=5, hydration w=4: $[K_2PtCl_4]=[FeCl_3]=2.5$ mmol/L and $[N_2H_4.H_2O]/[Fe^{3+}+Pt^{2+}]=40$ with reaction time from 0.25 h to 16 h (B); $[Fe^{3+/2+}] = [Pt^{2+}] = 2.5$ mmol/L and $N_2H_4.H_2O$ as reducing agent at ratio of $[N_2H_4.H_2O] / [Fe^{3+/2+} + Pt^{2+}] = 40$ and different precursors (C); $[K_2PtCl_4]=[FeCl_3]= 2.5$ mmol/L, $[N_2H_4.H_2O] / [Fe^{3+}+Pt^{2+}] = 40$ and $[NaBH_4]/[Fe^{3+}+Pt^{2+}] = 2.5$, 5 and 10 (D).

0.5 h when $FeCl_3$ and K_2PtCl_4 aqueous solutions are mixed together. These yellow crystals were characterized by XRD, and identified as K_2PtCl_6 (SI-Figure 10A).

SI-III.2. Structural Characterisations

Reaction time was varied from 0.25 h to 16 h to assess the effect of time on the Fe incorporation in the nPs. The XRD characterization is summarized in SI-Table 3 and the original XRD spectra can be found in SI-Figure 10B. Regardless of the time scale of the synthesis, there is no significant variation of the lattice constant or the composition. The 3.0 h and 16.0 h syntheses (111) peaks are sharper than observed with the 0.25 h sample which indicates larger nPs crystalline size in diameter. Crystalline grain size, as measured by XRD, increases slightly with the reaction time, whilst the TEM images presented in SI-

SI-Table 3. XRD data of FePt nPs synthesized at 30°C in isooctane, [Brij52] = 0.3 mol/L, [Brij52] / [butanol] = 5, w = 4, $[FeCl_3] = [K_2PtCl_4]$ = 2.5 mmol/L, $[N_2H_4.H_2O] / [Fe^{3+}+Pt^{2+}] = 40$. Reaction time ($t_r$), a is the lattice constant calculated based on (111), (200) and (220) peaks, x is the iron content in Fe_xPt_{1-x}, D_{XRD} is the crystalline grain size in diameter calculated based on FWHM of 3 different XRD peaks.

t_r (h)	a (Å)	x (%)	D_{XRD} (nm)
0.25	3.909 ± 0.004	14.6 ± 3.5	7.4 ± 1.4
3.00	3.910 ± 0.004	13.2 ± 3.6	7.3 ± 0.5
16.00	3.906 ± 0.001	15.3 ± 3.1	9.2 ± 1.0

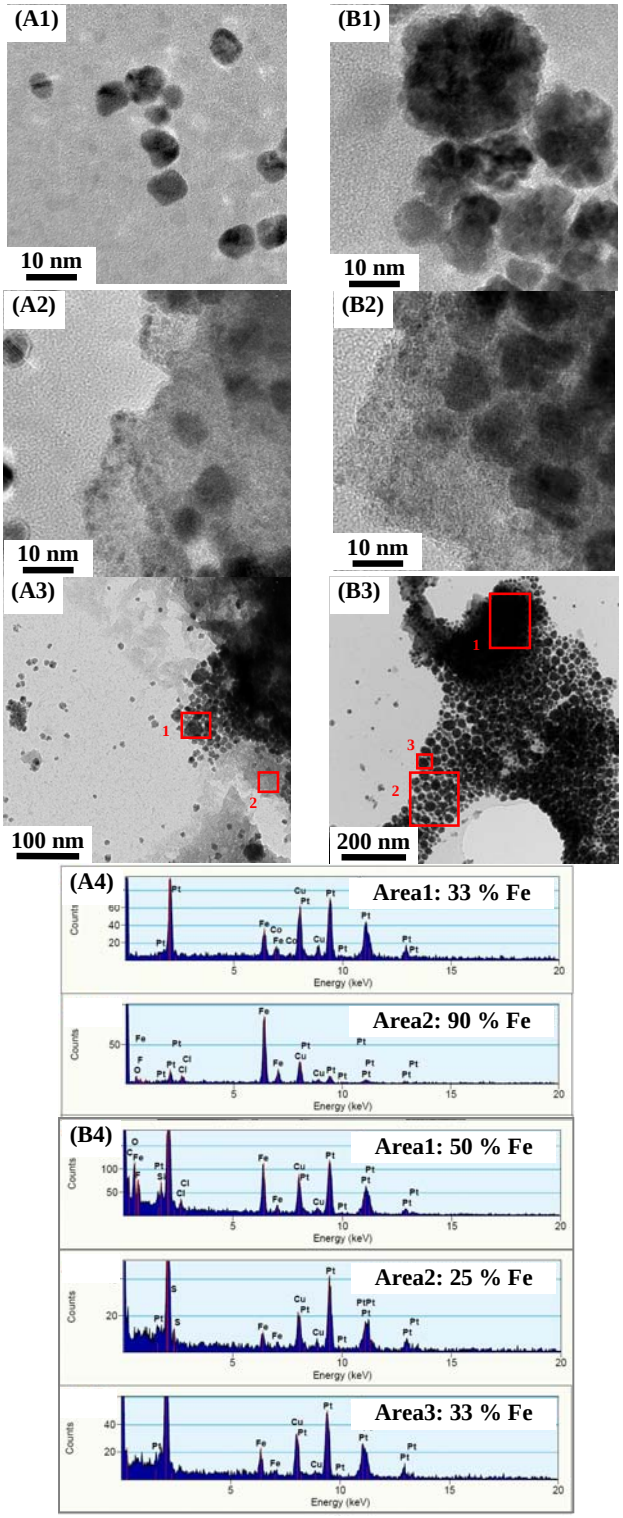

SI-Figure 11. FePt nPs synthesized at 30° C in isooctane, [Brij52] = 0.3 mol/L, [Brij52] / [butanol] = 5, w = 4, $[FeCl_3] = [K_2PtCl_4]$ = 2.5 mmol/L and $[N_2H_4.H_2O] / [Fe^{3+}+Pt^{2+}] = 40$. Reaction time 0.25 h (A) and 16 h (B). TEM data (1-2), bright field STEM picture (3) with red squares indicating areas analyzed by nanoSTEM-EDX and corresponding EDX spectra (4).

Figure 11 indicates that the particles are polydisperse and polydomain. After 15 min reaction, Pt rich nPs have already formed (SI-Figure 11A1). By increasing the reaction time to 16 h, the population of nPs larger than 10 nm is increased while the knobbly appearance of nPs is reinforced (SI-Figure 11B1). FePt

nPs with a higher contrast coexist with a film-like material of lower contrast (SI-Figure 11A2 and B2).

SI-Figure 11A3 and B3 present nanoSTEM-EDX data of FePt nPs synthesized with 0.25 h reaction time. The nPs formed within 15 mins contain about 30 % of Fe (SI-Figure 11A3 and A4, Area 1). More Fe was found in film material, as shown in SI-Figure 11A3 and A4. nPs synthesized with 16 h reaction shows similar composition results as 0.25 h sample. Film materials are Fe rich (SI-Figure 11B3 and B4, Area 1), and nPs show no obvious increase in the Fe content (SI-Figure 11B3 and B4, Area 1 and 3).

To summarize, EDX analysis is consistent with previous results, with a strong unhomogeneity of the chemical composition. No evidence of nPs with a Pt-rich core and Fe-rich shell was found. There is also no obvious increase in the Fe content of the nPs and the majority of reacted Fe exists in ill-defined and film-like materials. Together, these results are consistent with a model where *i*) inhomogeneous nucleation and *ii*) particle size increases first through the growth of individual grains, and later through aggregation of individual grains explaining the appearance of the particles. Different reduction rate of Fe and Pt precursors could then contribute to the inhomogeneous distribution of Fe and Pt in the samples obtained by co-reduction.

The composition does not vary significantly when using different Fe and Pt precursors except when FePt nPs were synthesized with $FeCl_2/K_2PtCl_4$ which (111) peak has higher 2θ angle value (SI-Figure 10C).[5, 11] Compared with nPs obtained with $N_2H_4.H_2O$ as reducing agent, FePt nPs synthesized with $NaBH_4$ display much boarder peaks, which is associated with much smaller crystalline size of the nPs (SI-Figure 10D). More importantly, (111) peak $NaBH_4$ sample shifted to higher angles, associated with higher Fe content of the nPs composition.[5, 11] TEM and nanoSTEM-EDX data are presented in the main document.

SI-IV. Magnetic Properties

Magnetization measurements are presented in SI-Figure 12 and summarized in SI-Table 4. Regardless of the reducing agent, the nPs display super-paramagnetic properties. The *ZFC-FC* curves indicate a low blocking temperature of 30 K and 25 K for the nPs obtained with hydrazine and sodium borohydrate respectively (SI-Figure 12A and C). It is also noticeable that the *FC* magnetization curve of the nPs synthesized with $[N_2H_4.H_2O]$ does not saturate and does not reach saturation at temperatures below T_b (SI-Figure 12A) in contrast of the nPs obtained with $[NaBH_4]$ (SI-Figure 12C).

Weak ferromagnetic properties are also suggested by the 5 K hysteresis loop (SI-Figure 12B). The nPs magnetization does not saturate at 5 T but displays a weak coercivity of ~ 170 Oe and a remanent magnetization of ~ 0.22 emu/g (SI-Figure 12B insert). This behavior contrasts with the nPs synthesized with $[NaBH_4]$ which display a saturated the magnetic moment at 5 K at a relatively small magnetic field (SI-Figure 12D). However these nPs, despite the much higher Fe content in nPs, which is about 35 % Fe in composition, display neither coercitivity nor remanence magnetisation (SI-Figure 12D). This is attributed to the much smaller size of the nanoparticles obtained with $[NaBH_4]$, (SI-Table 4).

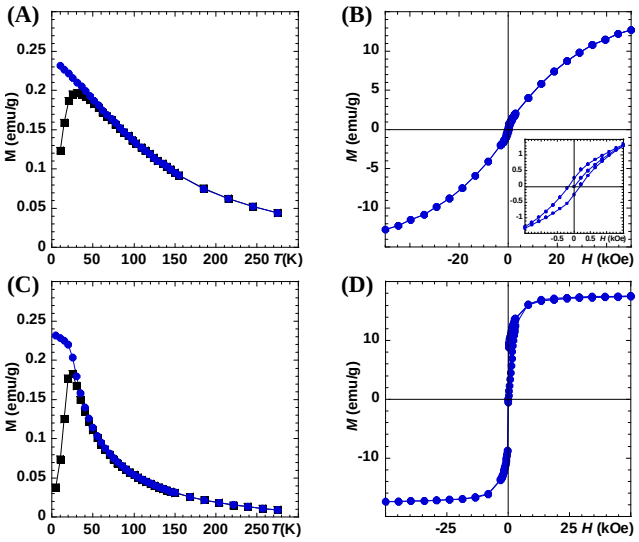

SI-Figure 12. FePt NPs synthesized at 30°C in isooctane, [Brij52] = 0.3 mol/L, [Brij52] / [butanol] = 5, hydration w = 4, $[FeCl_3]$ = $[K_2PtCl_4]$ = 2.5 mmol/L. (A, B) $[N_2H_4.H_2O]$ / $[Fe^{3+}+Pt^{2+}]$ = 40 and (C, D) $[NaBH_4]$ / $[Fe^{3+}+Pt^{2+}]$ = 5. (A, C) ZFC-FC magnetization curves obtained in a field 100 Oe, (B, D) Hysteresis loop at 5K.

SI-Table 4. Characterisation of FePt nPs: peak position (2θ), lattice constant (a), crystalline grain size (D_{XRD}) iron content (x) in Fe_xPt_{1-x}, blocking temperature (T_b), coercivity (H_c), magnetization at saturation (M_s), and remanent magnetization (M_r).

Reducing Agent	2θ (111) (degree)	a (Å)	D_{XRD} (nm)	x (-)	T_b (K)	H_c (Oe)	M_s (emu/g)	M_r (emu/g)
$[N_2H_4.H_2O]$	50.80 ± 0.01	3.909 ± 0.001	7.4 ± 0.1	14.8 ± 0.5	30	170	--	2.2
$[NaBH_4]$	51.14 ± 0.02	3.885 ± 0.002	3.5 ± 0.1	32.0 ± 1.3	25	--	17.6	--

References

1. S. Schrodle, R. Buchner and W. Kunz, *ChemPhysChem*, 2005, **6**, 1051-1055.
2. Ed.s E. Barsoukov, J. R. MacDonald and J. W. Sons, *Impedance Spectroscopy: Theory, Experiment and Applications*, New Jersey, 2005.
3. P. Atkins, Julio de Paula, *Physical Chemistry*, Oxford, 2006.
4. L. V. Azaroff, *Elements of x-ray crystallgraphy*, McGraw-Hill, Inc., 1968.
5. J. W. A. Bonakdarpour, D.A. Stevens, S. Sheng, T.L. Monchesky, R. Lo¨bel, R.T. Atanasoski, A.K. Schmoeckel, G.D. Vernstrom, M.K. Debe, J.R. Dahna,, *J. Electrochem. Soc.*, 2005, **152**, A61-72.
6. V. K. Pecharsky and P. Y. Zavalij, *Fundamentals of powder diffraction and structural characterization of materials*, Springer, New York, 2009.
7. K. M. Seemann, V. Baltz, M. MacKenzie, J. N. Chapman, B. J. Hickey and C. H. Marrows, *Physical Review B (Condensed Matter and Materials Physics)*, 2007, **76**, 174435.
8. C. M. Flynn, *Chem Rev*, 1984, **84**, 31-41.
9. D. R. Lide, R. C. Weast and C. R. Company., *CRC Handbook of Chemistry and Physics*, CRC Press, Boca Raton, Fla., 2002.
10. M. Takahashi, T. Ogawa, D. Hasegawa and B. Jeyadevan, *J. Appl. Phys.*, 2005, **97**, 10J307-301-306.
11. B. Stahl, J. Ellrich, R. Theissmann, M. Ghafari, S. Bhattacharya, H. Hahn, N. S. Gajbhiye, D. Kramer, R. N. Viswanath, J. Weissmuller and H. Gleiter, *Physical Review B (Condensed Matter and Materials Physics)*, 2003, **67**, 014422.